Functional rewiring across spinal injuries via biomimetic nanofiber scaffolds

Sadaf Usmani[a], Audrey Franceschi Biagioni[a], Manuela Medelin[a], Denis Scaini[a,b], Raffaele Casani[a], Emily R. Aurand[a], Daniel Padro[c], Ander Egimendia[c], Pedro Ramos Cabrer[c,e], Manuela Scarselli[f], Maurizio De Crescenzi[f], Maurizio Prato[d,e,g,1], and Laura Ballerini[a,1]

[a]Neurobiology Department, International School for Advanced Studies (SISSA/ISAS), Trieste 34136, Italy; [b]Nano Innovation Laboratory, ELETTRA Synchrotron Light Source, Trieste 34149, Italy; [c]Molecular Imaging Unit, Center for Cooperative Research in Biomaterials (CIC biomaGUNE), Basque Research and Technology Alliance (BRTA), San Sebastian 20014, Spain; [d]Bionanotechnology Unit, CIC biomaGUNE, BRTA, San Sebastian 20014, Spain; [e]Ikerbasque, Basque Foundation for Science, Bilbao 48009, Spain; [f]Department of Physics, University of Rome Tor Vergata, Rome 00133, Italy; and [g]Department of Chemical and Pharmaceutical Sciences, University of Trieste, Trieste 34127, Italy

Edited by John A. Rogers, Northwestern University, Evanston, IL, and approved September 4, 2020 (received for review March 27, 2020)

The regrowth of severed axons is fundamental to reestablish motor control after spinal-cord injury (SCI). Ongoing efforts to promote axonal regeneration after SCI have involved multiple strategies that have been only partially successful. Our study introduces an artificial carbon-nanotube based scaffold that, once implanted in SCI rats, improves motor function recovery. Confocal microscopy analysis plus fiber tracking by magnetic resonance imaging and neurotracer labeling of long-distance corticospinal axons suggest that recovery might be partly attributable to successful crossing of the lesion site by regenerating fibers. Since manipulating SCI microenvironment properties, such as mechanical and electrical ones, may promote biological responses, we propose this artificial scaffold as a prototype to exploit the physics governing spinal regenerative plasticity.

carbon-based nanomaterials | biomedical engineering | spinal cord lesion

Unlike lower vertebrates, adult mammals do not readily regenerate axons across spinal-cord injury (SCI), notwithstanding the high degree of post-SCI molecular and synaptic reorganization in intrinsic spinal circuits (below and above the lesion) leading to spontaneous, albeit limited, fiber sprouting (1–3). This post-SCI plasticity (4) represents a key biological substrate recently exploited by numerous treatments, including neuroprosthetic multisystems, to maximize axonal regrowth, ultimately to bypass the dysfunctional area (3–6). Combinatorial strategies to promote regenerative plasticity and behavioral recovery may depend upon engineering new-generation implants; namely, regenerative interfaces, able to artificially recruit axons to restore connectivity. Revolutionary advances in central nervous system (CNS) interfacing technology have required the development of nanomaterials (7, 8) and the design of visionary bioactive three-dimensional (3D) nanostructures to govern post-SCI plasticity and regeneration (9). Nanostructures incorporated in regenerative scaffolds may provide physical cues crucial to direct axonal growth and development, via appropriate mechanical, topological, and electrical stimulations (10). In the effort to recreate by artificial porous structures the physical complexity of the extracellular microenvironment, the use of conductive nanomaterials may be relevant, in particular when engineering electrically propagating tissues (11). In this scenario, multiwalled carbon nanotubes (MWCNTs) merge excellent physicochemical properties, especially mechanical and electrical ones, combined to biomimetic features (12, 13) and were recently engineered in 3D scaffolds [3D carbon nanofiber (CNF) (14)]. Three-dimensional CNF may allow for studying the dependence of axon regeneration and directionality on pure material physical properties, such as mechanical ones, in the absence of specific binding effects or of surface biomimetic and biochemical sophistications (10).

In biological systems in vitro, 3D CNF once bio-integrated with rodent spinal axons enabled the successful reconnection of cultured spinal cord segments (15). MWCNTs were exploited in in vitro models of CNS circuits to govern genuine biological processes, such as synapse formation, axon growth, and excitability (16–19), blurring the interface between natural and synthetic systems. The translation of such an in vitro ability to guide axonal rewiring in preclinical SCI models in vivo has not been addressed.

Results and Discussion

To induce SCI in mammals, we used the lumbar hemisection-paradigm (20) in adult rats, consisting in a hemicordectomy at the L1 level on the right side of the spinal cord, creating a ∼2 mm-long longitudinal lesion (*SI Appendix*). Our treatment, (sketched in Fig. 1*A*), consisted in the implantation, contextual to the surgery lesion (21–23), of 3D CNF scaffolds to reconstruct a favorable regenerative environment after injury to be compared to non-CNF implanted [polyethylene glycol (PEG), see below] SCI animals. Scanning electron microscopy (SEM) micrograph and high magnification confocal (reflection mode; Movie M1) 3D reconstructions of CNF in Fig. 1*B* visualize the random skeleton and the appearance of the interconnected MWCNTs, while the plot (Fig. 1*B*) shows the probability distribution of their outer diameter. CNF are very light (6 mg cm^{-3} density), hydrophobic (>150° contact angle), and conductive (about 30 Ω cm^{-1} electrical resistance) 3D scaffolds

Significance

Nanotechnology and neurobiology combined efforts might succeed in the design of hybrid microsystems that, once functionally integrated into the nervous tissue, might help in healing the injured spinal cord. A substantial challenge in this area is the development of structural scaffolds favoring spinal cord reconstruction. The future success of such smart devices resides also in the use of nanomaterials exploiting spinal microenvironment physical properties, such as mechanical and electrical ones, and their potential in promoting axonal regeneration. We synthesized an artificial scaffold based on nanomaterials with the necessary characteristics to guide axonal rewiring. The translational potential of introducing physics rules to neural tissue repair strategies was tested by implanting such a scaffold in spinal cord injury animal models.

Author contributions: M.P. and L.B. conceived the idea; L.B. designed research; S.U., A.F.B., M.M., D.S., R.C., E.R.A., D.P., A.E., and P.R.C. performed research; M.S. and M.D.C. contributed new reagents/analytic tools; S.U., A.F.B., M.M., D.S., R.C., E.R.A., D.P., A.E., and P.R.C. analyzed data; and L.B. wrote the paper.

The authors declare no competing interest.

This article is a PNAS Direct Submission.

[1]To whom correspondence may be addressed. Email: ballerin@sissa.it or prato@units.it.

This article contains supporting information online at https://www.pnas.org/lookup/suppl/doi:10.1073/pnas.2005708117/-/DCSupplemental.

that can be compressed up to values as high as 75% without showing sizeable irreversible deformation, with MWCNTs displaying large inner channel (115 ± 10 nm), and a high number of walls (160 ± 20; see SEM high magnification in the inset, Fig. 1*B*) (24).

The implant consisted of a sharp-pointed cylinder (trimmed to fit the SCI cavity, 1.79 ± 0.37 mm length and 0.76 ± 0.11 mm in diameter) of CNF (14, 15) that was embedded in a water-soluble, biocompatible, polymer (PEG; 100%). PEG encapsulation preserved the structural integrity of the very elastic, ultra-light weight, and porous CNF during implantation in SCI animals. Sham SCI animals were either not implanted or implants were represented by PEG cylinder without CNF (see *Methods* and *SI Appendix*, *Methods*).

After implantation, CNF scaffold integrity and its interaction with the injured tissue were assessed by SEM and, at macroscopic level, by MRI in sham SCI (named PEG group) and CNF animals (Fig. 1). In Fig. 1*C*, SEM micrographs of a spinal section containing the CNF implant (6 mo postsurgery) are shown. Fig. 1*C* (high magnification) illustrates the tight contacts between the CNF and the tissue surrounding the lesion. The CNF (14, 15) stability in freely moving SCI animals was further shown by confocal microscopy (Fig. 1 *C*, *Right*) with β-tubulin III [a neuron-specific marker (15)] positive processes suggesting scaffold invasion by neuronal fibers (15). Fig. 1*D* shows MRI high-resolution T2-weighted anatomical images of naïve (control) or SCI (PEG and CNF, 6 mo postsurgery) rats, allowing inspection of the entire spinal cord. In the naïve-animal images, the dorsal, ventral, and the two lateral tracts (hypointense on MRI) are clearly visible and run continuously along the total length of the scanned spinal cord. Conversely, PEG and CNF animals were characterized by an interruption of the right fiber tracts. In PEG-treated SCI rats, we observed a partial collapsing of the spinal tissue surrounding the injury, resulting in irregular boundaries (25, 26). On the contrary, CNF provided mechanical stability to the lesion site and appeared as a highly hypointense (black) area on MRI images (Fig. 1 *D*, *Right* column). The structural stabilization of the SCI spinal cord by CNF was further sustained by the average values of the lesion's area, that had not expanded neither collapsed from the initial surgery (1.97 ± 0.26 mm^2; Fig. 1*E*) and was larger than in PEG rats (0.85 ± 0.1 mm^2). We qualitatively assayed CNF ability to improve the mechanical stability of SCI lesion by the finite element method (FEM). The SCI spinal cord was simulated as a viscoelastic material (27) (*SI Appendix*, Fig. S1) shaped as a cylinder centrally hemisected (Fig. 1*F*). We analyzed the effects of axial load (30 kPa) on the geometry and dimension of the SCI lesion in two conditions: 1) upon simulating PEG melting, by leaving the SCI lesion empty (Fig. 1 *F*, *Top*); 2) upon simulating CNF implantation, by filling the SCI lesion with an insert matching the mechanical properties of CNF (Fig. 1 *F*, *Bottom*). In Fig. 1*F*, the color-coded deformations highlight the ability of the implant to mechanically stabilize SCI lesion when under load.

We next investigated local tissue reactivity to lesion and implanted materials by fluorescence microscopy. Spinal-cord slices from SCI animals (n = 5 and 5, PEG and CNF; n = 5 and 7, PEG and CNF; n = 5 and 4, PEG and CNF; 2, 4, and 6 mo post-SCI, respectively) were double-immunolabeled with antibodies against a specific cytoskeletal component (glial fibrillary acidic protein, GFAP) (3, 15, 28, 29) to identify astrocytes and against ionized calcium-binding adapter molecule 1 (Iba-1) to visualize microglia (Fig. 1*G*) (15, 28). We monitored dynamically the time-dependent distribution of astrocyte reactivity by quantifying GFAP intensity (arbitrary units, a.u.) at fixed rostral and caudal distances from the lesion edge with respect to the time postsurgery (2, 4, and 6 mo). Fig. 1*H* shows the typical profile of GFAP intensity peaking in proximity of the lesion edge (28) (0 μm). A comparison between PEG and CNF groups indicated lack of higher GFAP reactivity to CNF; such a response was comparable or even lower to that induced by PEG [for example, at 0 μm (caudal edge) in CNF: from 6.4 ± 1 a.u. at 2 mo to 10.3 ± 1 a.u. at 6 mo; at 0 μm (caudal edge) in PEG: from 9.1 ± 1 a.u. at 2 mo to 13.5 ± 6 a.u. at 6 mo; Fig. 1*H*]. Iba-1-reactivity was similar in all tested conditions at 2 mo, regardless the rostral or caudal locations (box plots in Fig. 1*I*) and Iba-1 intensity (a.u.) within 4 mo returned close to the reference values [at 0 μm (caudal edge) in CNF: from 5.3 ± 1 a.u. at 2 mo to 1 ± 0.3 a.u. at 4 mo; at 0 μm (caudal) in PEG: from 5.1 ± 1 a.u. at 2 mo to 2 ± 1 a.u. at 4 mo]. This first set of experiments supported biocompatibility, integration with the spinal cord, and long-term stability of CNF upon chronic implantation in vivo (29).

In our earlier study, CNF instructed axon regrowth and signal transmission in explanted spinal segments in vitro (15). To determine whether in SCI, CNF chronic implants were a more permissive environment allowing axonal regeneration through the lesion site, we looked for the presence of regrowing β-tubulin III-positive axons at 6 mo post-SCI (PEG n = 25 fields, n = 2 animals, and CNF n = 120 fields, n = 5 animals). This β-tubulin isoform is constitutively expressed in all CNS neurons (30) and is crucial for an efficient axon regrowth (31). Fig. 2*A* shows confocal micrographs of PEG and CNF examples. In PEG (Fig. 2 *A Left*), the structural instability of the injured tissue precluded a reliable assessment of β-tubulin III-positive axons crossing the lesion (32) since, due to tissue displacement, β-tubulin III-positive shredded remains were mixed to spare fibers at the lesion site (Fig. 2 *A*, *Top* and *Bottom Left*, arrowheads). These features in PEG animals indicated a lack of intense axonal regeneration from the lesion boundaries. Conversely, in CNF, fibers at the site of the lesion were characterized by complex paths, a feature of regenerating axons (22) (Fig. 2*A*, CNF, right, top and bottom arrowheads and *SI Appendix*, Fig. S2). The regenerative potential of CNF was estimated with confocal reconstruction of β-tubulin III-positive processes (>20 μm) which, when intermingled with the implant, could reach the lesion epicenter (Fig. 2 *A–C* and *SI Appendix*, Fig. S2). In CNF, we detected positive axons sprouting from the lesion boundary into the scaffold in 74% fields (Fig. 2 *A–C*). β-tubulin III-positive axons at the CNF epicenter in 87.5% fields confirmed substantial regrowth (Fig. 2*C*). The neuronal processes penetrated the CNF, displaying an arborized morphology (Fig. 2 *A*, *Right*, arrowheads and *SI Appendix*, Fig. S2). In CNF scaffolds, we did not detect β-tubulin III-positive cell soma as well as neuronal nuclear antigen (NeuN)-positive nuclei within the scaffold upon 6 mo implantation (*SI Appendix*, Fig. S2).

Blood supply is a limiting factor of successful tissue repair after SCI. We specifically investigated the presence of blood vessels in CNF-implanted animals and we detected the presence of RECA-1 (a marker of mature vascular endothelial cells) (33) positive cells, indicating the ability of endothelial cells (33, 34) to colonize artificial implants. Confocal micrographs (Fig. 2*B*) illustrate angiogenesis with small blood vessels (close to β-tubulin III-positive processes) invading the CNF structure in 80% fields and reaching the CNF epicenter in 96% of cases (Fig. 2*C* and *SI Appendix*, Fig. S2). This result is important since dynamic microvascular changes play a crucial role in SCI repair (33) and angiogenesis falls concurrently with cystic cavity formation (34).

To investigate axon regeneration within the entire spinal cord, we used MRI for macroscopic qualitative lesion assessment, and diffusion weighted imaging (DWI) to quantify the presence of neuronal fibers crossing the CNF at 6 mo postsurgery (Fig. 2 *D* and *E*). MRI and DWI were used to calculate the fractional anisotropy (FA) (35) of naïve control (n = 2) and post-SCI (5 to 6 mo), PEG (n = 5), or CNF (n = 8) adult spinal cords (36) (Fig. 2 *D* and *E*). FA values (Fig. 2*E* bar plot) of intact white-matter (WM), gray-matter (GM) and cerebrospinal fluid (CSF) did not differ among control, PEG, and CNF rats (35). FA at the lesion site in PEG was close to that observed in isotropic CSF-filled areas

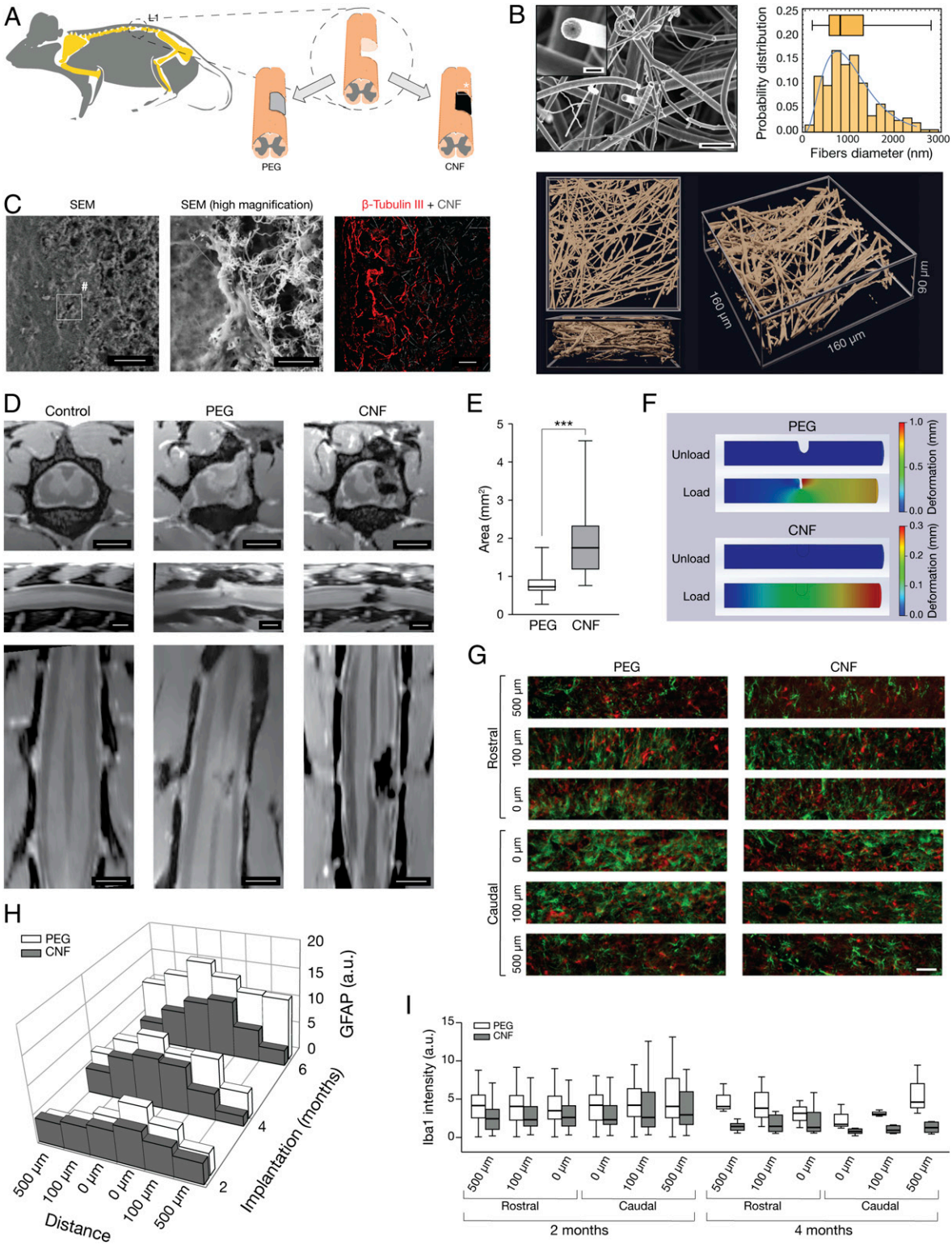

Fig. 1. CNF implanted in rat SCI. (*A*) Experimental setting. (*B*) High-magnification SEM micrographs (*Top*) and 3D confocal reconstruction (bottom; reflection mode, top and side projections) of CNF before implantation. Bar plot: probability distribution of MWCNTs diameter. SEM scales: 4 μm and 500 nm in the *Inset*. (*C*) Low (*Left*) and high (*Middle*) magnification SEM micrographs of CNF-implanted SCI spinal cord; scales, 40 μm and 1 μm, respectively. Confocal micrograph (*Right*) visualizing CNF by reflection mode and β-tubulin III-positive axons, same animal as above; scale, 50 μm. (*D*) MRI images (*Top* to *Bottom*; transverse, sagittal, and longitudinal sections); note the dark appearance of the CNF due to the porous nature of the implant; scales, 2 mm. (*E*) Box plot of the lesion dimension (***$P = 0.0006$). (*F*) FEM simulation of the viscoelastic deformation of a cylinder mimicking a spinal cord with the hemisected lesion left empty upon PEG dissolution (*Top*) or filled with an implant characterized by mechanical properties matching those of CNF (*Bottom*). (*G*) Immunofluorescence images taken at 0, 100, and 500 μm, rostral and caudal to the lesion edge, GFAP+ (green), and Iba-1+ (in red) neuroglia. Scale, 50 μm. (*H*) 3D plot and (*I*) box plots summarize GFAP and Iba-1 intensity average values.

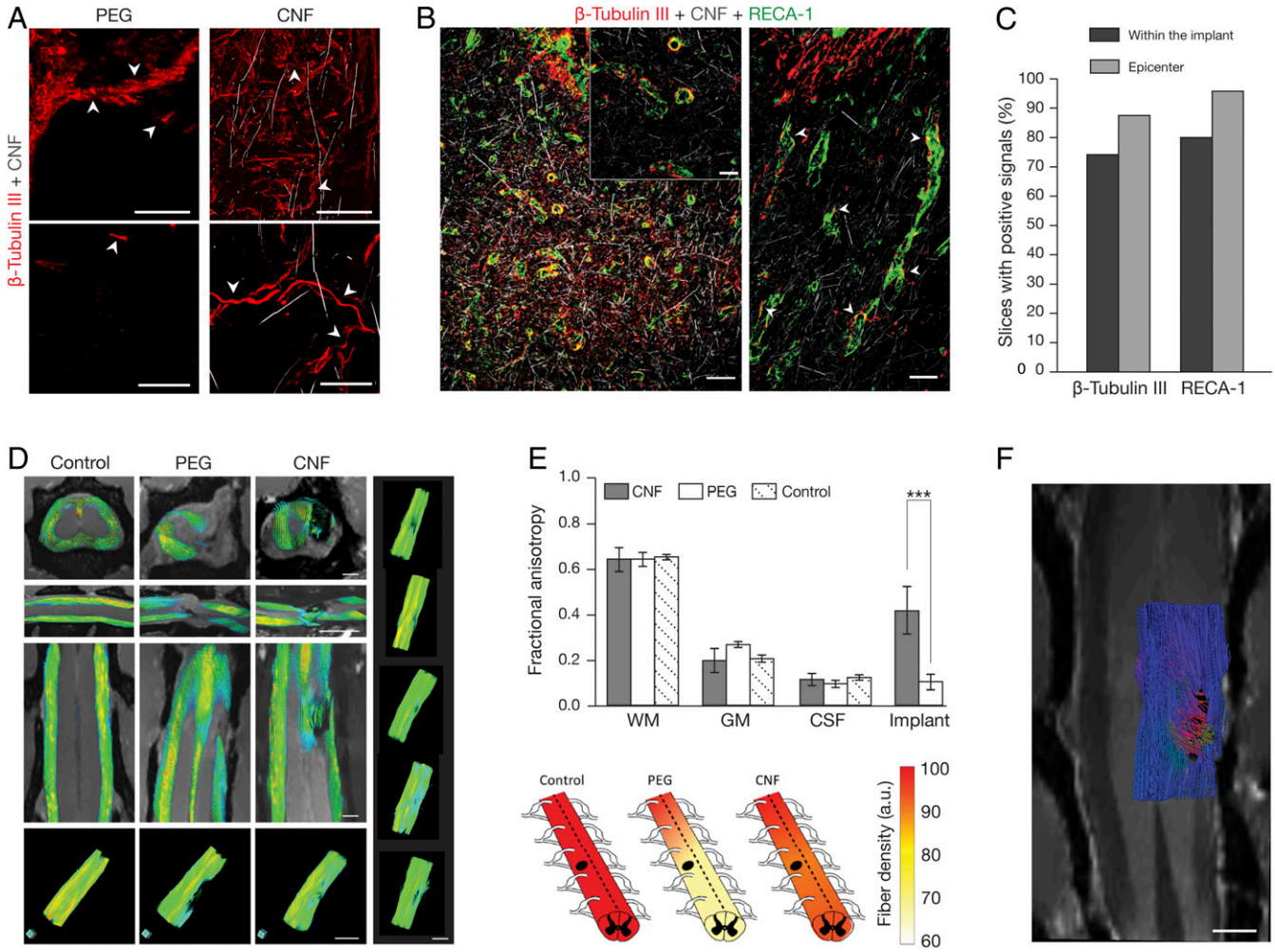

Fig. 2. CNF supports axonal regeneration. (*A*) Confocal micrographs detail the lesion site at low (*Top*) and high (*Bottom*) magnification. Arrowheads indicate shredded remains and fibers in PEG (*Left*) and tortuous axons within the CNF (*Right*). Scales top (*Left* and *Right*), 100 μm; bottom (*Left* and *Right*), 25 μm. (*B*) Low (*Left*) and high (*Inset* and *Right*) magnification of CNF-implanted spinal cord at the lesion site. Arrowheads indicate coexistence of β-tubulin III-positive fibers and RECA1-$^{+}$ blood vessels. Scale, left 100 μm, right and *Inset* 40 μm. (*C*) Quantification of fields with neurites or blood vessels traversing across and at the epicenter of the CNF. (*D*) Fiber tracks in aged-matched naïve (Control), and SCI (PEG and CNF) at 5 to 6 mo after surgery, FA values ranging from FA = 0 (in blue) to FA = 1 (in red). Right column: 3D representations of fiber tracts of five different examples of 5 to 6 mo CNT-implanted animals. Scales, 2 mm. (*E*, *Top*) FA, mean ± SD. *Bottom* heat plots of fiber density quantified from fiber tracking (***$P = 1.9\ e^{-05}$). (*F*) Fiber tracking analysis of DTI data constructed along the implant area of a CNF-treated rat (6 mo post-SCI; only half spine presented, to facilitate visualization), with the enclosed two-dimensional (2D) MRI coronal plane through the implant. Colors represent fiber orientation following conventional code for tensor directionality (blue: anterior-posterior, red: left-right and green: dorsal-ventral directions). Scale, 1 mm.

and significantly differed from the one in CNF, suggesting the presence of structured anisotropic matter inside the CNF, compatible with axonal fibers navigating through the scaffold.

DWI data were exploited to reconstruct fiber tracts along the spinal cords in multiple directions, using diffusion-tensor imaging (DTI) in combination with mathematical methods. The tracks obtained by this approach displayed shapes consistent with previous studies (36, 37). Fig. 2*D* shows color-coded fiber tracks reconstructed for spinal cords in aged-matched control, PEG, and CNF animals. At the lesion site, tracked fibers showed discontinuities in the dorsal, lateral, and ventral tracts of the PEG columns. Similar results were observed at 3D images of other sections for PEG animals. Conversely, CNF spinal cords showed the presence of fibers across the implant, strongly supporting the regrowth of axons between spinal sections rostral and caudal to the scaffold, trespassing through the CNF structure itself. Similar results obtained by the 3D graphical reconstruction presented in Fig. 2 *D* (*Bottom* and *Right*), using an alternative software package, confirmed the robustness of this evidence. We quantified the rostro-caudal gradient of fiber densities with respect to the lesion site (±3 mm) in the entire spinal cords (heat-plots, Fig. 2*E* and *SI Appendix*, *Methods*). In PEG animals, 33% of fibers were lost at the lesion site and such a reduction extended to 3 mm caudally, whereas only 12% of fiber loss was detected in CNF at the lesion site and this reduction was limited to 5% to 3 mm caudally. Thus, CNF scaffolds enabled extensive regrowth of axons crossing the spinal gap caused by SCI. To gain insights into fiber *XYZ*-orientations when grown within the CNF, we used a tractography algorithm (*SI Appendix*, *Methods*) to further exploit MRI and DTI imaging. Fig. 2*F* shows the 3D reconstruction of fibers crossing CNF in an implanted SCI rat (6 mo). Apparently, the CNF-crossing fibers grew through the MWCNTs scaffold following a coordinated path, reaching the rostral and caudal sides of the lesion site by merging multiple directions, suggestive of a role of the CNF structure in guiding the regenerated crossing fibers.

To investigate whether any regrowing axons represented regeneration of axotomized corticospinal tract (CST), we labeled CST by injecting the fluorescent dextran neurotracer (NTD) (3)

into primary motor/sensory cortex contralateral to the SCI lesion in a separate set of CNF-implanted rats ($n = 4$; Fig. 3 *A–C*). In CNF animals, NTD labeled long, thin axons all of the way through the contralateral spinal cord caudal to the lesion (Fig. 3*D*) as well as within the CNF (magnified panels in Fig. 3*E*, CNF in gray), thus crossing the lesion gap. This result hints at the contribution of CST to the population of regenerating axons penetrating the 3D scaffold. Further immunofluorescence labeling of β-tubulin III-positive processes within the CNF identified presynaptic vesicular glutamate transporter 1 (VGLUT1)-positive puncta (see example in Fig. 3*F*, arrowhead), used to label glutamatergic presynaptic terminals (38), supporting the presence of glutamatergic axons and the formation of glutamatergic synapses. We also detected positive labeling for 5-hydroxytryptamine (5-HT) in association with β-tubulin III-positive neurites (see example in Fig. 3*G*, arrowhead) regrown within the CNF. These results indicated the presence of specific types of axons (glutamatergic and serotoninergic) able to regenerate when supported by the implanted CNF.

Finally, to determine whether CNF scaffolds support functional recovery, animals were assessed using the Basso, Beattie, and Bresnahan (BBB) locomotor scale (39) up to 4 mo after surgery in PEG and CNF (Fig. 4*A*). The spinal cord (hemi) transection model adopted is characterized by a mild SCI with moderate locomotor impairment (*SI Appendix*, Fig. S3*D*); nevertheless, CNF animals exhibited significant functional recovery when compared to PEG ones. In all SCI animals, we observed the loss of locomotor function of the hindlimb ipsilateral to the lesion (24 h post-SCI). Locomotor performance of CNF animals ($n = 18$) at acute (1 d) and subacute (1 wk) stages from spinal injury showed significant improvement with early weight supported plantar stepping and regain of forelimb-hindlimb coordination in comparison with PEG ($n = 16$). This improvement in recovery was maintained up to the chronic spinal injury stage (4 mo; $n = 5$ CNF and $n = 6$ PEG) with weight support, limb coordination, and toe clearance in CNF.

Since the BBB test reflects locomotor behavior only, we sought to measure more refined sensory-motor functions like stepping, limb placement, and motor control using the ladder-beam test (40). At 24 h postsurgery, both groups ($n = 13$, PEG and $n = 8$, CNF) showed a clear drop in their sensory-motor ability, shown in Fig. 4*B*; indeed, PEG animals barely moved the affected limb (41), while CNF animals attempted to climb on the rung. In subacute (1 wk) and subchronic (29 d) SCI phases, CNF scaffolds led to a strong and significant improvement in functional recovery (Fig. 4*B*).

Footprint analysis (Fig. 4*D*) showed that the onset of plantar placement post SCI in PEG animals ($n = 8$) took days to develop, as opposed to CNF ($n = 9$) ones.

Our data suggested that CNF induced faster and improved locomotor long-term recovery in comparison to the PEG group, thus the CNF scaffold played an important role in motor behavior improvement.

Notwithstanding post-SCI plasticity and fiber sprouting, injured CNS axons are unable to regenerate (42) and transection models of SCI are designed to target neurorepair strategies potentials (43). This study exploits 3D MWCNTs as artificial implantable regenerative interfaces in SCI adult rats. CNF implants showed long-term bio-integration with limited tissue reactivity. Invasion of neuronal fibers and blood vessels within the implant was demonstrated by confocal immunohistochemistry and MRI, further supporting neurocompatibility and CNF material potential for SCI repair. The ability of CNF to guide axonal tracts regeneration across the SCI lesion was strengthened by MRI DTI reconstructions of the entire spinal cord, by in vivo neurotracing, and by the ex vivo observation of glutamate and serotonin-positive axons (44) within the MWCNTs porous structure. Numerous physical features of the CNF may have played a role in axonal regeneration, including the morphology of the MWCNTs self-standing skeleton, its mechanical, and elastic properties (24), enabling the scaffold to adapt and sustain spinal displacements with CNF integration into the spinal tissue. MWCNTs have also been reported to affect electrical activity in cultured neuronal axons (17) and we cannot exclude that the conductive properties of the scaffold may also augment synaptic plasticity (18); collectively, these CNF features may ultimately boost postinjury regeneration.

The improvement in locomotor function brought about by CNF in acute and subacute phases is suggestive of an abatement of post-SCI spinal shock, maybe due to the mere mechanical coupling of the implant with the neural tissue speeding up the successful management of acute SCI, typically characterized by edema or structural instability (25). Our FEM simulations supported this interpretation, showing in the absence of CNF a large SCI lesion deformation (fraction of mm) and huge stress accumulation at the SCI lesion boundaries (up to a hundred of kPa; *SI Appendix*, Fig. S1), potentially resulting in further spinal damage. Indeed, CNF stiffness (24, 45) values match very well the experimental values of rodent spinal cord compliance (46).

After incomplete SCI, most rats (PEG and CNF) showed substantial degrees of spontaneous recovery, presumably as a

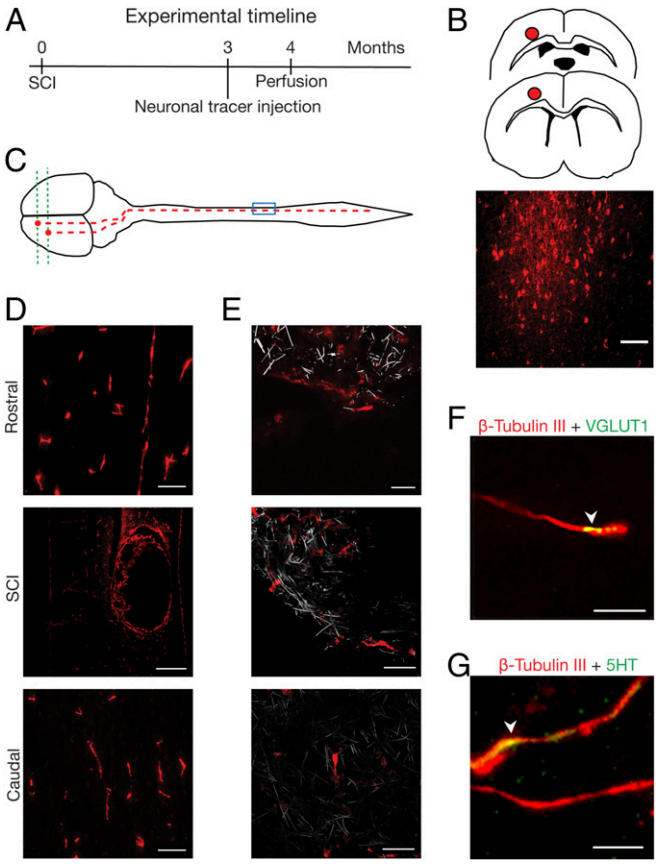

Fig. 3. Regenerated axons invading CNF originate from the motor/sensory cortex. (*A–C*) Schematic drawing of the site of microinjection and tracing (red dot) and fluorescent micrograph of dextran-labeled neurons at the motor cortex (coronal section) and (*D*) of labeled fibers in CNF-implanted spinal cord; scales, 100 μm, 500 μm, and 100 μm, rostral, SCI, and caudal, respectively. (*E*) confocal micrographs of dextran-positive fibers (red) growing within the CNF (in gray, reflection mode). Scales, 20 μm, 40 μm, and 40 μm, *Top*, *Middle* and *Bottom* respectively. (*F*) and (*G*) Within the CNF (4 to 5 mo post SCI, different animal than above; MWCNTs are not visualized), arrowhead indicates colocalization (in yellow) of β-tubulin III-positive fibers (in red) with $VGLUT_1$-positive puncta (in green), with 5-HT labeling (in green). Scales, 10 μm (*F*) and 5 μm (*G*).

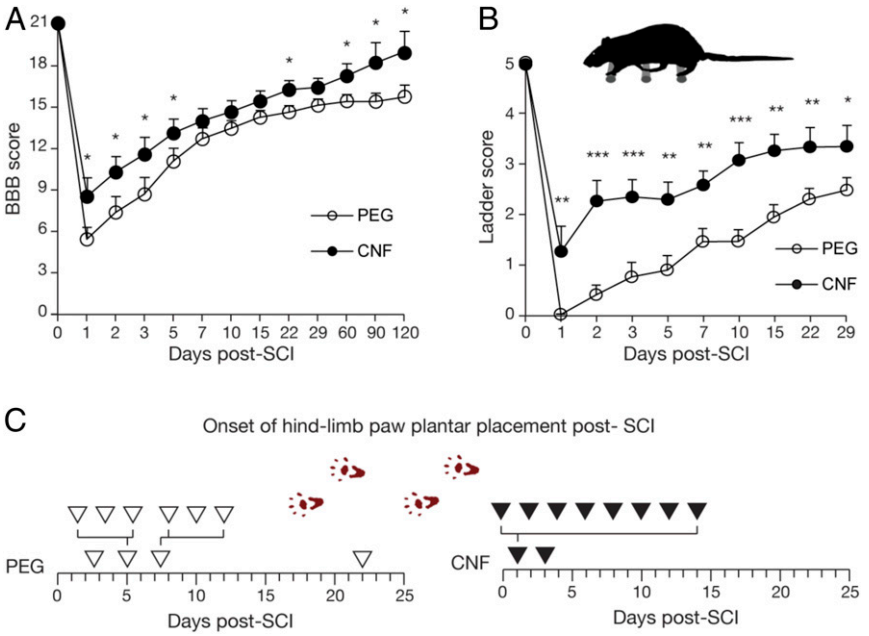

Fig. 4. Functional recovery in locomotor behavior. (*A*) Locomotor recovery measured by BBB rating scores. (*B*) Ladder-beam test shows performance scores against days postsurgery. (*C*) Postoperation onset of plantar placement assessed by footprint analysis. Arrowheads represent each animal. (*$P < 0.05$, **$P < 0.01$, ***$P < 0.001$.)

result of plasticity and compensatory sprouting of surviving neurons (1–4). Indeed, in SCI models similar to the one we adopted, sprouting or adaptation of spared fibers were proposed to contribute to post-SCI plasticity and partial recovery (42). However, the complexity of shaping axonal regeneration in spinal cord repair is challenging and might not match functional outcomes (47).

CNF promoted a significant recovery in locomotor and sensory-motor behavior (48) also in subchronic and chronic (49) SCI animals. While previous work (3) showed long-term functional recovery sustained by delivery of promoters of propriospinal axons regrowth, the current study indicates that CNF scaffold physical features help to improve locomotor activity in subchronic and chronic post-SCI phases likely via increased axon regeneration. We suggest that pure MWCNTs engineered in 3D scaffolds provide an artificial extracellular microenvironment with a remarkable ability to guide neuronal regrowth in vivo.

In conclusion, the regenerative capability of the adult spinal cord to reorganize its circuits when altering the lesion physical microenvironment by smart materials might represent a key tool to synergize the therapeutic potentials of current technological approaches to SCI (4).

Materials and Methods

All *Materials and Methods* are reported in detail within the *SI Appendix* and briefly summarized below.

Materials and Preparation of Implants. MWCNTs were obtained from Prof. Maurizio De Crescenzi's laboratory (14, 24). As previously reported (15), this MWCNT scaffold (CNF) is a freestanding 3D framework of self-assembled MWCNTs. Further material details are reported within the *SI Appendix, Methods*.

Surgical Procedures and Animal Care. Fifty-eight adult female Wistar rats (age 2 to 3 mo) were recruited for lumbar spinal hemisection model. Unilateral L1-L2 spinal hemisection model was utilized to produce a partial spinal-cord lesion (20). Surgeries were performed in a randomized manner and the two, PEG and CNF, or three, lesion alone PEG and CNF, groups were performed on the same day to minimize differences or surgical bias among groups. Further surgery details are reported within the *SI Appendix, Methods*.

Scanning Electron Microscopy. Details are reported within the *SI Appendix, Methods*.

Finite Element Simulation of the Spinal Cord. Details are reported within the *SI Appendix, Methods*.

Magnetic Resonance Imaging. Magnetic Resonance Imaging studies were conducted at 11.7 Tesla using a Bruker Biospec USR 117/16 MRI system (Bruker Biospin GmbH) with actively shielded gradients of 750 mT/m power and a slew rate of 6660 T/m/s. Radiofrequency (RF) transmission was achieved by using a quadratic transmit volumetric coil of 72 mm of internal diameter (Bruker T1148V3), and RF reception was achieved with a surface coil (Bruker T11657V3) of ~2 cm of diameter. Further MRI details are reported within the *SI Appendix, Methods*.

Dextran Tracing. Details are reported within the *SI Appendix, Methods*.

Behavioral Studies. Open field observation of hindlimb locomotor recovery was assessed by using the BBB rating scale (39). Skilled motor behavior was assessed by the ladder-beam test by grading stepping, limb placing, and motor control on each rung, on a scale from 0 to 5. Baseline recording was taken 24 h before surgery. Further behavior details are reported within the *SI Appendix, Methods*.

Data Analysis, Statistics, and Reproducibility. All values from samples subjected to the same experimental protocols were pooled together and expressed as mean ± SE, unless otherwise indicated, with n = biologically independent experiments, usually number of animals, unless otherwise indicated. Levene's or D'Agostini's test was used to assess the homogeneity of variances. Statistically significant difference between two data sets was assessed by one-tailed Student's t test for parametric data and by Mann–Whitney for nonparametric ones. Statistical significance was determined at $P < 0.05$. Significance was graphically indicated as follows: *$P < 0.05$, **$P < 0.01$, ***$P < 0.001$. In box plots, the thick horizontal bar indicates the median value, while the boxed area extends from the 25th to 75th percentiles with the whiskers ranging from the fifth to the 95th percentiles.

Data and Materials Availability. The data that support the findings of this study are all available in the main paper or in the *SI Appendix*. Individual values that support the plots within this paper are available in the SISSA Neuron technology and Physiology Lab repository upon reasonable request to the corresponding author. All study data are included in the article and supporting information.

ACKNOWLEDGMENTS. We are grateful to M. Grandolfo and G. Baj for microscopy assistance, G. Leanza for setting the lesion paradigm, M. Gigante and M. Giugliano for biomechanical simulations, and we are indebted to A. Nistri for helpful discussion and revision of the text. This work was funded by the European Union's Horizon 2020 Research and Innovation Programme under Grant Agreement 737116 (to L.B). M.P., as the recipient of the AXA Bionanotechnology Chair, is grateful to the AXA Research Fund for financial support. M.P. was also supported by the Spanish Ministry of Economy and Competitiveness MINECO (project CTQ2016-76721-R), the University of Trieste, and the Spanish State Research Agency (Maria de Maeztu Units of Excellence Program Grant MDM-2017-0720).

1. O. Raineteau, M. E. Schwab, Plasticity of motor systems after incomplete spinal cord injury. *Nat. Rev. Neurosci.* **2**, 263–273 (2001).
2. R. G. Dickson, V. K. Lall, R. M. Ichiyama, Enhancing plasticity in spinal sensorimotor circuits following injuries to facilitate recovery of motor control. *Curr. Opin. Physiol.* **8**, 152–160 (2019).
3. M. A. Anderson *et al*., Required growth facilitators propel axon regeneration across complete spinal cord injury. *Nature* **561**, 396–400 (2018).
4. G. Courtine, M. V. Sofroniew, Spinal cord repair: Advances in biology and technology. *Nat. Med.* **25**, 898–908 (2019).
5. V. M. Tysseling-Mattiace *et al*., Self-assembling nanofibers inhibit glial scar formation and promote axon elongation after spinal cord injury. *J. Neurosci.* **28**, 3814–3823 (2008).
6. I. R. Minev *et al*., Biomaterials. Electronic dura mater for long-term multimodal neural interfaces. *Science* **347**, 159–163 (2015).
7. Z. Luo, D. E. Weiss, Q. Liu, B. Tian, Biomimetic approaches toward smart bio-hybrid systems. *Nano Res.* **11**, 3009–3030 (2018).
8. G. Hong, X. Yang, T. Zhou, C. M. Lieber, Mesh electronics: A new paradigm for tissue-like brain probes. *Curr. Opin. Neurobiol.* **50**, 33–41 (2018).
9. C. Lu *et al*., Flexible and stretchable nanowire-coated fibers for optoelectronic probing of spinal cord circuits. *Sci. Adv.* **3**, e1600955 (2017).
10. K. Franze, J. Guck, The biophysics of neuronal growth. *Rep. Prog. Phys.* **73**, 094601 (2010).
11. T. Dvir, B. P. Timko, D. S. Kohane, R. Langer, Nanotechnological strategies for engineering complex tissues. *Nat. Nanotechnol.* **6**, 13–22 (2011).
12. D. Scaini, L. Ballerini, Nanomaterials at the neural interface. *Curr. Opin. Neurobiol.* **50**, 50–55 (2018).
13. S. Marchesan, L. Ballerini, M. Prato, Nanomaterials for stimulating nerve growth. *Science* **356**, 1010–1011 (2017).
14. L. Camilli *et al*., Pressure-dependent electrical conductivity of freestanding three-dimensional carbon nanotube network. *Appl. Phys. Lett.* **102**, 183117 (2013).
15. S. Usmani *et al*., 3D meshes of carbon nanotubes guide functional reconnection of segregated spinal explants. *Sci. Adv.* **2**, e1600087 (2016).
16. N. A. Kotov *et al*., Nanomaterials for neural interfaces. *Adv. Mater.* **21**, 3970–4004 (2009).
17. G. Cellot *et al*., Carbon nanotubes might improve neuronal performance by favouring electrical shortcuts. *Nat. Nanotechnol.* **4**, 126–133 (2009).
18. G. Cellot *et al*., Carbon nanotube scaffolds tune synaptic strength in cultured neural circuits: Novel frontiers in nanomaterial-tissue interactions. *J. Neurosci.* **31**, 12945–12953 (2011).
19. A. Fabbro *et al*., Spinal cord explants use carbon nanotube interfaces to enhance neurite outgrowth and to fortify synaptic inputs. *ACS Nano* **6**, 2041–2055 (2012).
20. A. Roozbehi *et al*., Age-associated changes on axonal regeneration and functional outcome after spinal cord injury in rats. *Acta Med. Iran.* **53**, 281–286 (2015).
21. J. Koffler *et al*., Biomimetic 3D-printed scaffolds for spinal cord injury repair. *Nat. Med.* **25**, 263–269 (2019).
22. Y. D. Teng *et al*., Functional recovery following traumatic spinal cord injury mediated by a unique polymer scaffold seeded with neural stem cells. *Proc. Natl. Acad. Sci. U.S.A.* **99**, 3024–3029 (2002).
23. S. Liu, Y. Y. Xie, B. Wang, Role and prospects of regenerative biomaterials in the repair of spinal cord injury. *Neural Regen. Res.* **14**, 1352–1363 (2019).
24. L. Camilli *et al*., A three-dimensional carbon nanotube network for water treatment. *Nanotechnology* **25**, 065701 (2014).
25. E. Moeendarbary *et al*., The soft mechanical signature of glial scars in the central nervous system. *Nat. Commun.* **8**, 14787 (2017).
26. A. Domínguez-Bajo *et al*., Myelinated axons and functional blood vessels populate mechanically compliant rGO foams in chronic cervical hemisected rats. *Biomaterials* **192**, 461–474 (2019).
27. J. T. Maikos, Z. Qian, D. Metaxas, D. I. Shreiber, Finite element analysis of spinal cord injury in the rat. *J. Neurotrauma* **25**, 795–816 (2008).
28. K. Zhou *et al*., Graphene functionalized scaffolds reduce the inflammatory response and supports endogenous neuroblast migration when implanted in the Adult Brain. *PLoS One* **11**, e0151589 (2016).
29. M. A. Anderson *et al*., Astrocyte scar formation aids CNS axon regeneration. *Nature* **532**, 195–200 (2016).
30. A. Latremoliere *et al*., Neuronal-specific TUBB3 is not required for normal neuronal function but is essential for timely axon regeneration. *Cell Rep.* **24**, 1865–1879.e9 (2018).
31. C. Conde, A. Cáceres, Microtubule assembly, organization and dynamics in axons and dendrites. *Nat. Rev. Neurosci.* **10**, 319–332 (2009).
32. J. M. Cregg *et al*., Functional regeneration beyond the glial scar. *Exp. Neurol.* **253**, 197–207 (2014).
33. M. Oudega, Molecular and cellular mechanisms underlying the role of blood vessels in spinal cord injury and repair. *Cell Tissue Res.* **349**, 269–288 (2012).
34. D. N. Loy *et al*., Temporal progression of angiogenesis and basal lamina deposition after contusive spinal cord injury in the adult rat. *J. Comp. Neurol.* **445**, 308–324 (2002).
35. S. Madi, K. M. Hasan, P. A. Narayana, Diffusion tensor imaging of in vivo and excised rat spinal cord at 7 T with an icosahedral encoding scheme. *Magn. Reson. Med.* **53**, 118–125 (2005).
36. Y. Cohen, D. Anaby, D. Morozov, Diffusion MRI of the spinal cord: From structural studies to pathology. *NMR Biomed.* **30**, e3592 (2017).
37. T. E. Conturo *et al*., Tracking neuronal fiber pathways in the living human brain. *Proc. Natl. Acad. Sci. U.S.A.* **96**, 10422–10427 (1999).
38. N. P. Pampaloni *et al*., Single-layer graphene modulates neuronal communication and augments membrane ion currents. *Nat. Nanotechnol.* **13**, 755–764 (2018).
39. D. M. Basso, M. S. Beattie, J. C. Bresnahan, A sensitive and reliable locomotor rating scale for open field testing in rats. *J. Neurotrauma* **12**, 1–21 (1995).
40. G. A. Metz, I. Q. Whishaw, The ladder rung walking task: A scoring system and its practical application. *J. Vis. Exp.* **28**, 1204 (2009).
41. S. Rossignol, G. Barrière, O. Alluin, A. Frigon, Re-expression of locomotor function after partial spinal cord injury. *Physiology (Bethesda)* **24**, 127–139 (2009).
42. M. Ballermann, K. Fouad, Spontaneous locomotor recovery in spinal cord injured rats is accompanied by anatomical plasticity of reticulospinal fibers. *Eur. J. Neurosci.* **23**, 1988–1996 (2006).
43. T. Cheriyan *et al*., Spinal cord injury models: A review. *Spinal Cord* **52**, 588–595 (2014).
44. M. Ueno *et al*., Corticospinal circuits from the sensory and motor cortices differentially regulate skilled movements through distinct spinal interneurons. *Cell Rep.* **23**, 1286–1300.e7 (2018).
45. X. Ge *et al*., Flexible carbon nanofiber sponges for highly efficient and recyclable oil absorption. *RSC Adv.* **5**, 70025–70031 (2015).
46. M. Fournely, Y. Petit, E. Wagnac, M. Evin, P.-J. Arnoux, Effect of experimental, morphological and mechanical factors on the murine spinal cord subjected to transverse contusion: A finite element study. *PLoS One* **15**, e0232975 (2020).
47. P. Lu *et al*., Motor axonal regeneration after partial and complete spinal cord transection. *J. Neurosci.* **32**, 8208–8218 (2012).
48. R. U. Ahmed, M. Alam, Y. P. Zheng, Experimental spinal cord injury and behavioral tests in laboratory rats. *Heliyon* **5**, e01324 (2019).
49. A. N. Leszczyńska, H. Majczyński, G. M. Wilczyński, U. Sławińska, A. M. Cabaj, Thoracic hemisection in rats results in initial recovery followed by a late decrement in locomotor movements, with changes in coordination correlated with serotonergic innervation of the ventral horn. *PLoS One* **10**, e0143602 (2015).